ADVANCED FUNCTIONAL MATERIALS
www.afm-journal.de

Compositionally Modulated Magnetic Epitaxial Spinel/Perovskite Nanocomposite Thin Films

*Dong Hun Kim, Nicolas M. Aimon, Xueyin Sun, and Caroline A. Ross**

There is great interest in self-assembled oxide vertical nanocomposite films consisting of epitaxial spinel pillars in a single crystal perovskite matrix, due to their tunable electronic, magnetic, and multiferroic properties. Varying the composition or geometry of the pillars in the out-of-plane direction has not been previously reported but can provide new routes to tailoring their properties in three dimensions. In this work, ferrimagnetic epitaxial $CoFe_2O_4$, $MgFe_2O_4$, or $NiFe_2O_4$ spinel nanopillars with an out-of-plane modulation in their composition and shape are grown in a $BiFeO_3$ matrix on a (001) $SrTiO_3$ substrate using pulsed laser deposition. Changing the pillar composition during growth produces a homogeneous pillar composition due to cation interdiffusion, but this can be suppressed using a sufficiently thick blocking layer of $BiFeO_3$ to produce bi-pillar films containing for example a layer of magnetically hard $CoFe_2O_4$ pillars and a layer of magnetically soft $MgFe_2O_4$ pillars, which form in different locations. A thinner blocking layer enables contact between the top of the $CoFe_2O_4$ and the bottom of the $MgFe_2O_4$ which leads to correlated growth of the $MgFe_2O_4$ pillars directly above the $CoFe_2O_4$ pillars and provides a path for interdiffusion. The magnetic hysteresis of the nanocomposites is related to the pillar structure.

1. Introduction

Recently considerable research has been carried out on the remarkable tunability of the magnetic, ferroelectric, and multiferroic properties of complex oxides via their interfaces.[1–4] Although interfaces are usually oriented parallel to the substrate in thin film heterostructures, thin films consisting of a codeposited perovskite (e.g., $BiFeO_3$ (BFO), $BaTiO_3$ (BTO), and $PbTiO_3$ (PTO)) and a spinel (e.g., $CoFe_2O_4$ (CFO), $MgFe_2O_4$ (MFO), and $NiFe_2O_4$ (NFO)) can form nanocomposites[1,5–8] in which vertical (i.e., out-of-plane) pillars of one oxide grow within a matrix of the other, both of which are epitaxial with respect to the substrate, leading to well defined vertical oxide interfaces. The substrate is typically a perovskite such as $SrTiO_3$.

Among many perovskite and spinel nanocomposite combinations, BFO–CFO has been at the center of attention because of its two-phase multiferroic behavior that originates from strain-coupling between magnetostrictive ferrimagnetic CFO (magnetostriction constant, $\lambda_{100,\mathrm{CFO}} = (-250 \text{ to } -590) \times 10^{-6}$[9]) and piezoelectric BFO (piezoelectric coefficient, $d_{33,\mathrm{BFO}} \approx 60$ pm V^{-1} at 200 nm film thickness[10]).[11,12] The magnetic hysteresis curves of a BFO–CFO nanocomposite on a (001) $SrTiO_3$ substrate typically show out-of-plane anisotropy due to the combination of magnetoelastic anisotropy from the out-of-plane contraction of the CFO lattice along the vertical direction caused by the lattice mismatch with the BFO matrix, and shape anisotropy from the rod-like shape of the CFO pillars. However, CFO is a hard magnetic material with relatively high magnetocrystalline anisotropy ($K_1 \approx 3 \times 10^6$ erg cm^{-3}) and magnetostriction. It is useful to be able to control the magnetic anisotropy and switching field in order to optimise the film for a range of applications, for example, to maximize the energy product for hard magnetic films, or to lower the power consumption for multiferroic memory devices,[13] by varying the composition or geometry of the spinel pillars.

One way to vary the magnetic properties is to modulate the composition of the spinel pillars along their length, producing for example a pillar with a hard and a soft layer. Nanocomposite or bi-layer thin films made from exchange-coupled soft and hard magnetic materials show an enhanced remanence and large magnetic energy product,[14–18] exceeding what is expected from the components without exchange coupling.[19] Several groups have reported hysteresis loop tuning and magnetization reversal in exchange-coupled ferromagnetic hard/soft bilayers by changing the thicknesses and magnetic properties of the layers.[20,21] An analogous behavior may be anticipated in a compositionally-modulated "bi-pillar" made from both hard CFO and soft MFO or NFO. However, high diffusivity within spinels has impeded the formation of compositionally-modulated spinel films despite fabrication at relatively low temperatures of 350–450 °C.[22–25]

In this article, we report on the fabrication of epitaxial spinel pillars from layered CFO, MFO, and NFO in a perovskite BFO matrix by combinatorial pulsed laser deposition (CPLD), and an investigation of their morphology, strain state and magnetic properties. Cation interdiffusion in the spinel pillars could be prevented by using a blocking layer of BFO to produce epitaxial nanocomposites containing separated pillars of different spinel

---

Dr. D. H. Kim, N. M. Aimon, Dr. X. Sun,
Prof. C. A. Ross
Department of Materials Science and Engineering
Massachusetts Institute of Technology
Cambridge, MA, USA
E-mail: caross@mit.edu

DOI: 10.1002/adfm.201302844

composition. Magnetic hysteresis is determined by the magnetic coupling between the hard and soft spinel pillars and was tuned by controlling the thickness and separation of spinel pillars of different compositions. The methods described here produce vertical nanocomposites with a modulation in the composition, location and/or width of the pillars, providing strategies for control in the out-of-plane direction. This is the first report of multilayering in epitaxial spinel-perovskite nanocomposites, though structures such as BTO/CFO layered dots grown using porous alumina have been described.[26]

2. Results and Discussion

We first describe nanocomposites with homogeneous pillar compositions. **Figure 1**a–c shows the top view SEM images of BFO–CFO, BFO–MFO, and BFO–NFO composites ≈ 120 nm thick fabricated with CPLD. We have reported that CPLD produces a linear composition gradient as a function of distance not only in the BFO–CFO system but also in different oxide systems as a result of the thickness gradient produced by off-axis deposition.[27,28] The samples spanned a distance of 5 cm with a spinel-rich composition at one end and perovskite-rich at the other. At the spinel-rich end of the nanocomposite (Figure 1a-1,b-1, c-1), the BFO matrix did not fully surround the spinel pillars and some partly exposed pillars are visible. As the BFO content increased, spinel nanopillars are seen with a faceted structure in which {110} planes form the sides, and four low-energy[29,30] {111} planes and one {001} plane form the cap of the pillars, within a BFO matrix that covered the whole area between the pillars. At this deposition condition, the width of the spinel pillars was 20–50 nm which is much smaller than the film thickness and suggests that the vertical strain in the spinel imposed by the BFO matrix would be dominant over the strain imposed by epitaxial growth on the substrate.[31] The top view shape of the spinel pillars became more rounded for BFO-rich BFO–MFO and BFO–NFO compared to BFO–CFO (Figure 1a-5,b-5,c-5).

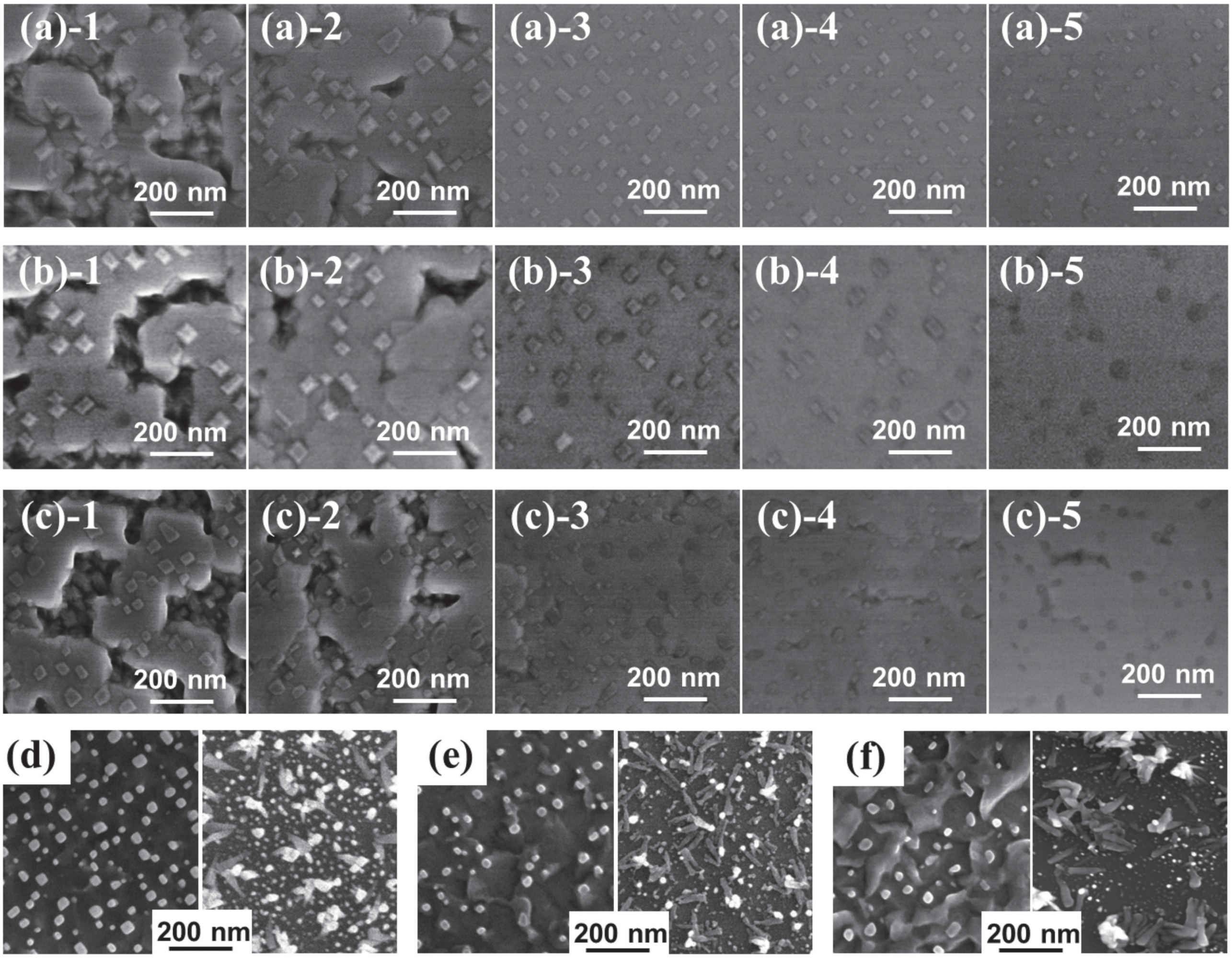

Figure 1. a–c) Top-view SEM images of a) BFO–CFO, b) BFO–MFO, and c) BFO–NFO nanocomposites on (001) STO substrate fabricated by CPLD. Each series becomes increasingly rich in BFO from sample 1 (left) to 5 (right). d–f) Top view SEM images after etching the third sample of each series with HCl solution for 30 seconds (left) and 180 s (right) for d) BFO–CFO, e) BFO–MFO, and f) BFO–NFO. The small features in the right hand images represent spinel nuclei that did not form pillars, or unetched BFO.

To examine the pillar morphology of the BFO-rich nanocomposites, the samples were dipped in HCl which is a good selective chemical etchant for BFO without etching spinel.[28,32] A 30 s etch (left images in Figure 1d–f) removed surface BFO leaving supported pillars, while a 180 s etch (right images) released the pillars completely. Pillars show a partly rounded cross section after etching, which may be caused by slow etching of the pillars, but it can also occur to minimize surface energy as seen in the BTO–CFO system.[33,34]

According to one dimensional XRD patterns (not shown), all the peaks present could be attributed to perovskite and spinel phases without any secondary phases. In the magnified XRD pattern around the STO (002) peak (Figure S1, Supporting Information), it is seen that the spinel nanopillars were under compressive out-of-plane strain while the BFO matrix was under tensile strain. The tensile strain of BFO and the compressive spinel strain increased with increasing BFO content. Figure S2 (Supporting Information) gives HRXRD analyses of the detailed structure and strain states of the third samples of each series of Figure 1 which showed well facetted spinel pillars and complete BFO coverage. Four-fold symmetry of STO, BFO, and spinel phases in the φ scans indicates epitaxial growth of both phases on the substrate.

The out-of-plane lattice parameters and strains for each series of samples are given in Table S1 in the Supporting Information, from one dimensional XRD. Although the ratio of the out of plane lattice parameter of the spinels to twice that of the BFO approached closer to unity as the BFO content increased, the lattice parameters did not match even for the highest BFO content samples. There was partial strain relaxation (e.g., misfit dislocations) along the vertical interfaces, that is, the interfaces were semi-coherent.

Figure 2a–c shows reciprocal space maps of BFO–CFO, BFO–MFO, and BFO–NFO nanocomposites respectively around the asymmetric STO (103) peak for the third sample of each series. The alignment of the BFO and STO peaks along the in-plane reciprocal direction q_x indicates that the BFO phase was strained to match the substrate but the large extent of the spot suggests partial strain relaxation, and the spinel (026) reflections are barely observable due to their low intensity. Table S2 (Supporting Information) gives the corresponding data for both the in-plane and out-of-plane lattice parameters. The c/a ratio and unit cell volume are also listed. The unit cell volumes are in reasonable agreement with the bulk values. Differences between the unit cell volumes of the films and for bulk materials may be a result of non-conservation of unit cell volume with varying strain[35] or differences in oxygen vacancy concentration between the films and bulk.

The spinel phases in the three samples of Figure 2 and Table S2 (Supporting Information) showed a c/a ratio of 0.998 for CFO and MFO and 0.999 for NFO, that is, the unit cells were only slightly compressed in the out of plane direction. The

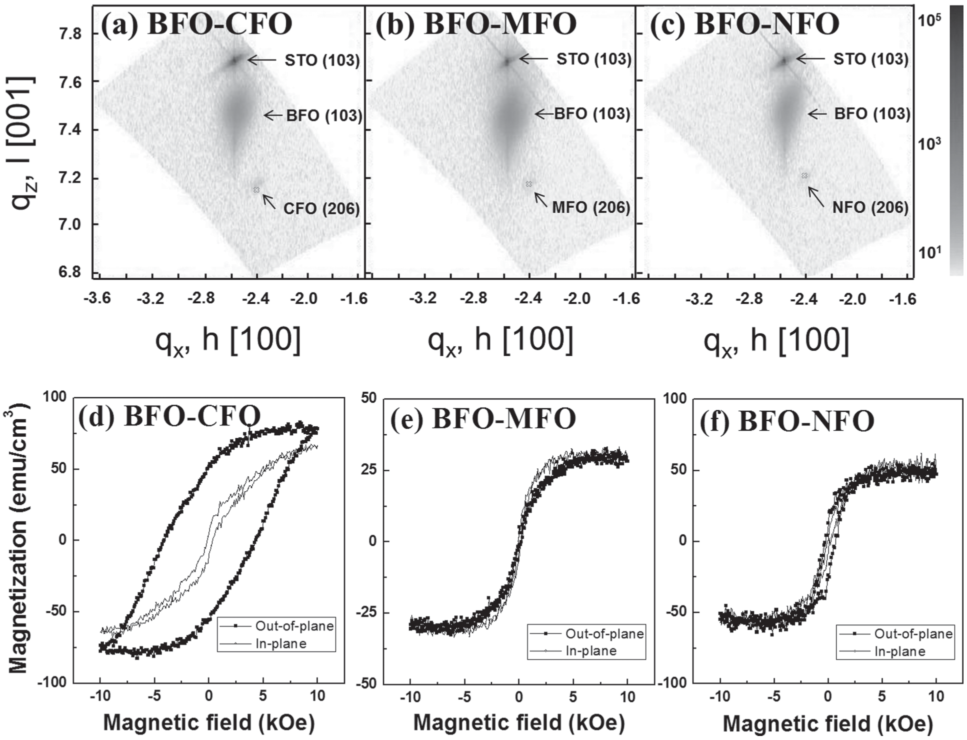

Figure 2. a–c) X-ray reciprocal space maps of BFO–CFO, BFO–MFO, and BFO–NFO nanocomposites for the asymmetric (103) reflection of BFO and STO and the (206) reflection of spinel. The vertical and horizontal axes are in-plane [100] and out-of-plane [001] directions. The red crosses denote the bulk peak positions of spinel phases. The intensity is on a log scale shown by the scale bar at the right. d–f) In-plane and out-of-plane hysteresis loops of MFO–BFO nanocomposite thin films deposited at 5 mTorr oxygen pressure and 650 °C within the applied magnetic field range of –10 kOe to +10 kOe. Note the different y-axis scale for (e).

relaxation in NFO agrees with a previous report by HRTEM at the interface of $[\mathrm{BiFeO}]^{4+}/[\mathrm{Ni,Fe]O_2}]^{1.5-}$.[5] In the three samples the BFO phase was under in-plane compression with a c/a ratio of 1.021, 1.027 and 1.015 for BFO–CFO, BFO–MFO, and BFO–NFO respectively.

Figure 2d–f shows the magnetic hysteresis loops of the films corresponding to Figure 2a–c, and additional magnetic data for other composites are given in Figure S3 (Supporting Information). The magnetization values were calculated averaged to the entire film volume due to difficulty calculating the spinel volume fraction for the BFO-rich and the BFO-poor samples, where the BFO either partly covers the spinel pillars or is discontinuous. However, assuming in the third sample of each series that the pillars are vertical prisms, each nanocomposite contains 25% volume fraction of spinel according to its area fraction; and neglecting the facetted tops of the pillars which have heights of 12–15 nm, the saturation magnetizations are quite reasonable compared to the bulk values of saturation magnetization: $M_{\mathrm{s\ CFO,bulk}}$ = 400 emu cm^{-3},[28] $M_{\mathrm{s\ MFO,bulk}}$ = 130 emu cm^{-3},[8] and $M_{\mathrm{s\ NFO,bulk}}$ = 270 emu cm^{-3}.[36]

The BFO–CFO nanocomposite showed hard magnetic behavior and could not be saturated with the field available from the VSM, 10 kOe. The measurement therefore represents a minor loop and the saturation magnetization and coercivity are lower bounds. The out-of-plane magnetic anisotropy of the CFO is greater than the shape anisotropy would predict (of order 2.5 kOe)[28] and is attributed to magnetoelastic anisotropy.[28,37] A rough calculation of the total anisotropy field (H_{tot}) of a CFO pillar includes shape (H_{sh}) and magnetoelastic (H_{me}) terms, that is, $H_{\mathrm{tot}} = H_{\mathrm{sh}} + H_{\mathrm{me}}$, where $H_{\mathrm{sh}} = 2\pi M_{\mathrm{s}}$, and $H_{\mathrm{me}} = \frac{3\lambda_{001} Y \varepsilon_{001}}{M_{\mathrm{s}}}$ where λ_{001} is the magnetostriction coefficient, Y is Young's modulus (141.6 GPa), and ε_{001} is the compressive strain along the vertical direction (–0.0032 from the one dimensional XRD, which had higher intensity peaks and better strain accuracy than HRXRD). This predicts H_{sh} and H_{me} of 2.5 kOe and 8.5–20.1 kOe, respectively. Even though the strain was small, the large magnetostriction of CFO ensured a significant magnetoelastic contribution to the anisotropy.

BFO–MFO and BFO–NFO nanocomposites were magnetically softer, with lower saturation moments compared to BFO–CFO. In BFO–MFO, the magnetic hysteresis is insensitive to strain because MFO has only a small magnetostriction coefficient, $\lambda_{\mathrm{MFO,polycrystalline}} = -6 \times 10^{-6}$.[38] In BFO–NFO the magnetoelastic anisotropy is negligible because the NFO phase is relaxed, even though NFO has a moderate magnetostriction constant, $\lambda_{\mathrm{NFO}} = -45.9 \times 10^{-6}$.[39] The shape anisotropy of an infinite pillar of NFO would be 1.7 kOe, leading to an out of plane easy axis.

We now demonstrate the stacking of magnetically soft MFO or NFO pillars above CFO in a BFO matrix. Changing the spinel target part way through the deposition was expected to produce "bi-pillars" with a composition modulation along their length. First, BFO–CFO nanocomposites were grown, then BFO–MFO (**Figure 3**a) or BFO–NFO (Figure 3d) were deposited by ablating the MFO or NFO instead of the CFO target at the same growth conditions without interrupting the growth. The BFO–(CFO/MFO) samples showed square or rectangular facetted spinel pillars but BFO–(CFO/NFO) showed a more irregular pillar cross-section and a few {001} facets were observed, indicated by arrows in Figure 3d. Removing the BFO matrix showed that the pillars were continuous through the film thickness (left of Figure 3a), but it was difficult to identify the presence of separate CFO and MFO or NFO regions of the pillars from the HRXRD because of low peak intensity. (The dotted red lines in Figure 2b,e present the peak positions of CFO, MFO, and NFO pillars for the third sample of each series in Figure 1 for comparison, showing that these peaks are close together.) However, the BFO (002) reflection in the BFO–(CFO/MFO) nanocomposite showed two peaks corresponding to out-of-plane lattice constants of 4.052 and 4.024 Å (Figure 3b). These two different strain states are attributed to the two different layers of the BFO codeposited with the CFO and MFO. On the other hand, the BFO phase in BFO–(CFO/NFO) had only one peak corresponding to 4.004 Å (Figure 3e).

The in-plane and out-of-plane hysteresis curves of the bi-pillar nanocomposites were not a superposition of the loops of BFO–CFO and BFO–NFO or BFO–MFO. The loops did not show separate steps corresponding to the reversal of hard and soft phases, but instead showed a smooth though broad switching process. Both bi-pillar nanocomposites were magnetically hard like the BFO–CFO, and the out-of-plane hysteresis loops were not saturated at 10 kOe, so the loops of Figure 3c,f are minor loops. The BFO–(CFO/NFO) loop resembled that of BFO–CFO whereas the BFO–(CFO/MFO) had a lower coercivity and a higher saturation moment. The higher moment is likely a consequence of more complete saturation of the BFO–(CFO/MFO) under the available field of 10 kOe.

TEM samples of the pillars of composition CFO/MFO were obtained by etching the film with HCl for 180 s to fully dissolve the BFO and placing the pillars on a carbon film coated copper grid. Figure 3g shows the magnified images of the bottom (left image, expected to be CFO) and top (right image, MFO) of one bi-pillar. In the left image, the inter-planar distances were 1.48 and 1.47 Å and the planes made a 60 degree angle, well matched with the $\{40\bar{4}\}$ planes of CFO with a zone axis of [111]. In the right image, two planes with inter-planar spacing of 2.09 and 2.11 Å exhibited a perpendicular alignment, which corresponds to the {400} planes of MFO. The insets are selected area diffraction patterns. The similar lattice constant of CFO and MFO makes it difficult to determine the composition of the ends of the pillar, but there was no indication of a sharp boundary between the phases.

Figure 3h shows EDS spectra for the CFO–MFO bi-pillar. Bi was not observed due to the selective etching of the BFO, but carbon and copper from the grid were detected. The analysis shows a similar composition for the CFO and MFO ends of the pillar indicating considerable interdiffusion of the Mg and Co within the pillar, in contrast to the perovskite-spinel interface at which interdiffusion is suppressed.[34,40] This interdiffusion within the pillar therefore formed a spinel phase of (Co,Mg)$\mathrm{Fe_2O_4}$ [or (Co,Ni)$\mathrm{Fe_2O_4}$] with properties that were intermediate between the soft MFO [or NFO] and hard CFO phases. A high deposition temperature, highly energetic PLD plume,[41] and the many unoccupied sites in the spinel structure all contribute to interdiffusion during the growth of the films.

CFO and NFO have an inverse spinel structure consisting of $\mathrm{Fe}_A(\mathrm{CoFe})_B\mathrm{O}_4$ or $\mathrm{Fe}_A(\mathrm{NiFe})_B\mathrm{O}_4$ with A and B representing the tetrahedral and octahedral sites, whereas MFO has a partially inverse spinel structure of $\left(\mathrm{Mg}^{2+}_{1-x}\mathrm{Fe}^{3+}_{x}\right)_A\left(\mathrm{Mg}^{2+}_{x}\mathrm{Fe}^{3+}_{2-x}\right)_B\mathrm{O}_4$.

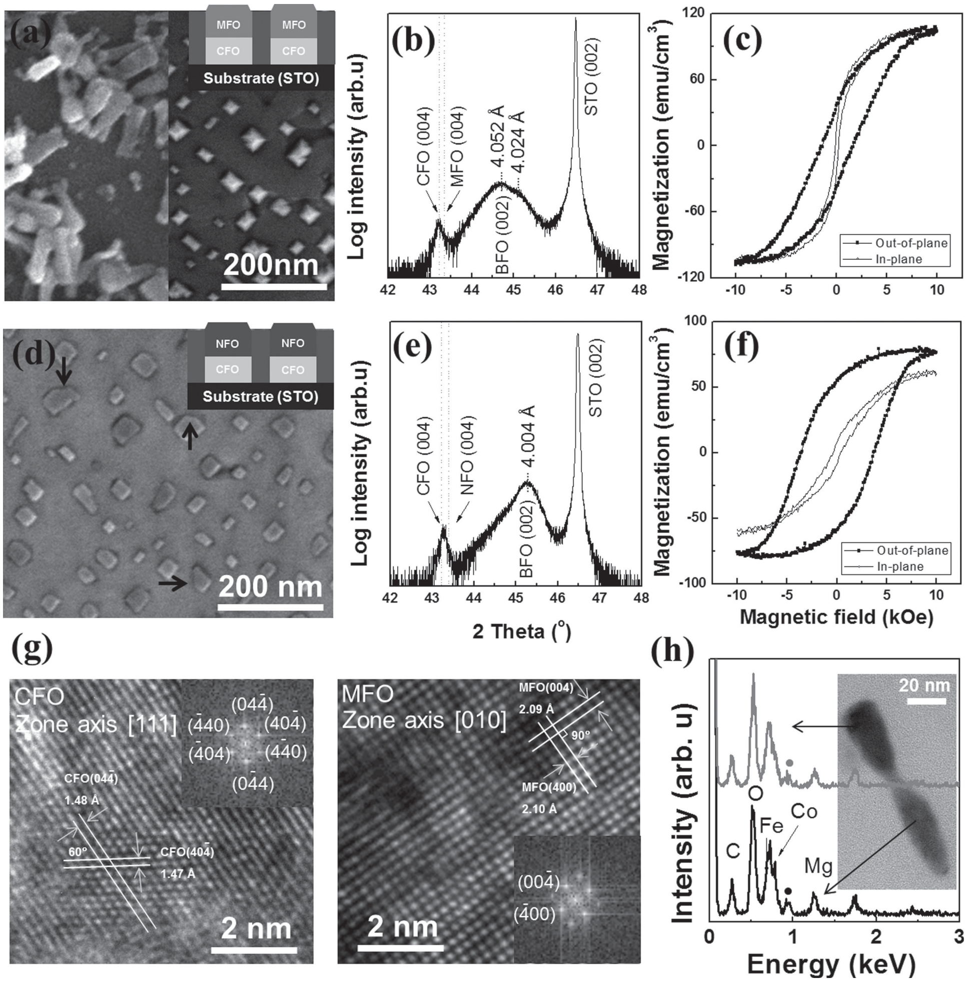

Figure 3. a) Top view SEM (right), b) magnified XRD pattern around the (002) STO peak, and c) in-plane and out-of-plane magnetic hysteresis loops of a BFO–(CFO/MFO) bi-pillar sample. The left SEM image in (a) was taken after dipping in HCl for 180 s. d–f) SEM, XRD, and magnetic hysteresis loops of BFO–(CFO/NFO) bi-pillar samples. g) HRTEM images of two different parts in a CFO/MFO bi-pillar after etching with HCl. Insets are selected area electron diffraction (SAED) of each area. h) EDS spectra of two different parts in CFO/MFO bi-pillar. Inset is BFO-etched CFO/MFO bi-pillars taken by TEM. The closed circle is the peak of Cu.

In the spinel structure, only eight of the tetrahedral sites and half of the octahedral sites are occupied, promoting cation migration.[42] Cation diffusion has been reported not only at the spinel/spinel interface[43] but also at the interface between a CFO film and an MgO substrate.[44] Interdiffusion of Mg^{2+} from the MFO into the *A* and *B* sites of CFO dilutes the Co^{2+} in the CFO, decreasing saturation magnetic moment, and anisotropy. Ni^{2+} has lower anisotropy than Co^{2+} and the $(Co,Ni)Fe_2O_4$ formed by interdiffusion has magnetic properties intermediate between those of CFO and NFO.

Samples were made for comparison in which the order of growth was reversed, that is, the NFO or MFO was grown first then the CFO. The overall shapes of the magnetic hysteresis loops were similar to samples where CFO was grown first, with out of plane easy axis, but the coercivities were higher and the magnetic moment at 10 kOe was lower because the samples were harder to saturate. Data is given in Figure S4, Supporting Information. The interdiffusion of Mg and Co was still present for the two different growth sequences.

To avoid interdiffusion and provide more latitude for varying the magnetic properties, deposition at low energy and temperature was conducted. The microstructure and magnetic properties of the composites were unaffected for the available range of laser fluence of 2.0–3.3 J cm^{-2} for the optimum deposition temperature of 650 °C. However, a deviation from the optimum deposition temperature induced dramatic effects on nanocomposite formation. At 600 °C the spinel-perovskite nanocomposite formed but the saturation moment was lower. At 560 °C the BFO formed both the cubic and a metastable tetragonal phase, and at 480 °C tetragonal BFO and iron oxide formed. Another approach to prevent interdiffusion was to use either MgO or $MgAl_2O_4$ (MAO) barrier layers between the two spinel compositions, but the BFO-(CFO/MgO/MFO) nanocomposite formed only within a very small window of deposition parameters and the BFO–(CFO/MAO/MFO) system did not show clear phase separation.

To provide an effective diffusion barrier within the spinel pillars, a BFO layer was introduced part way through the

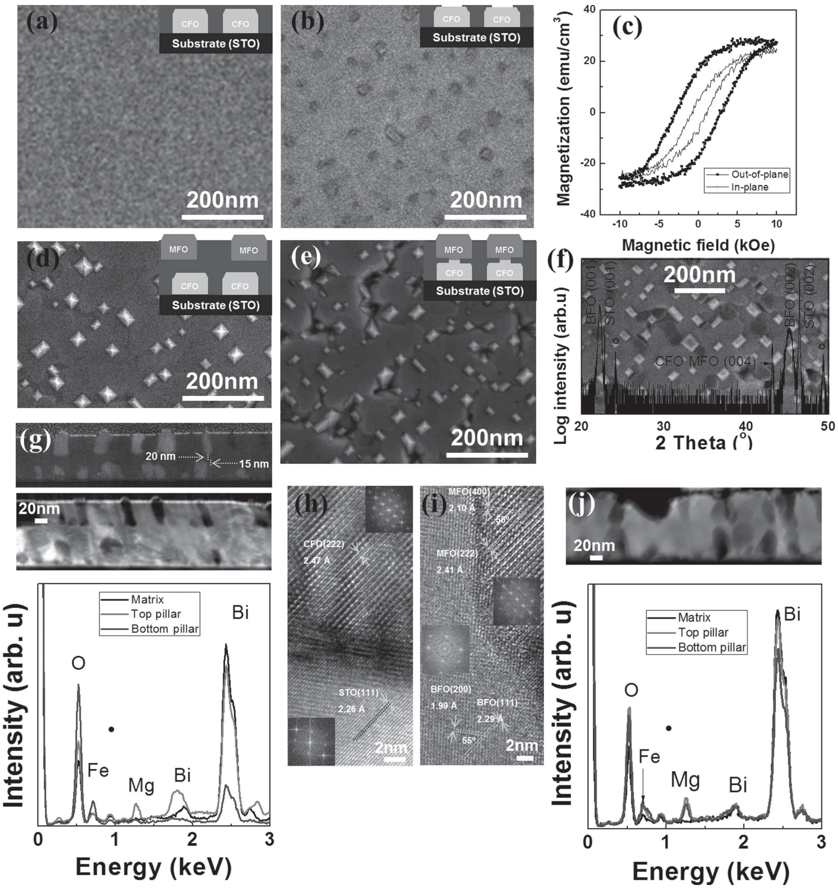

Figure 4. Top view SEM images of a) 35 and b) 15 nm BFO thin films on BFO–CFO nanocomposites. The 35 nm film completely covers the pillars. The insets show the structures schematically. c) Magnetic hysteresis loops of BFO–CFO with 35 nm BFO cap. d,e) Top view SEM images of BFO–MFO nanocomposite grown on (a,b), respectively. The insets show the structures schematically. f) Top view SEM image of a thicker BFO–(CFO/BFO/MFO) bi-pillar nanocomposite in which an additional dark phase shows, and its XRD pattern. g) The top and middle images are cross-sectional SEM and low magnification Z-contrast images of the BFO–(CFO/35 nm BFO/MFO) bi-pillar nanocomposite, respectively. The bottom figure gives EDS spectra of regions centered on the BFO blocking layer, the MFO, and the CFO pillars. The • symbol indicates the Cu signal from the TEM grid. (h,i) are high resolution TEM images of the STO/CFO and BFO/MFO interface in BFO–(CFO/35 nm BFO/MFO) by BFO cut by FIB along [110]. Insets in the TEM images are fast Fourier transforms (FFT) of selected area electron diffraction. j) Z-contrast image and elemental analysis of BFO-(CFO/15 nm BFO/MFO) nanocomposite in which the CFO and MFO pillars are in contact.

formation of the nanocomposite to cover the tops of the pillars. Various thicknesses of BFO layers were deposited on BFO–CFO (Figure S5, Supporting Information) to investigate the morphology. When the BFO layer was thick, ≈25 nm or more, BFO covered the film and spinel pillars were not visible (**Figure 4**a). For thinner BFO the facetted tops of the spinel pillars could be seen (Figure 4b). Though the pillars protrude 12–15 nm above the BFO matrix, the tops of the pillars were not buried until the BFO blocking thickness reached 25 nm; the BFO initially covered the edge of the pillars as shown in the inset of Figure 4b and then finally covered the whole area as in the inset of Figure 4a. Sakamoto et al. reported BFO growth on spinel $(Fe,Zn)_3O_4$ (FZO) particles at 650 °C and showed that the FZO was surrounded by BFO when the FZO particles were below 500 nm diameter.[45,46] Because the width of the pillars (20–50 nm) in our system is much smaller than the critical terrace width for nucleation, BFO did not nucleate on top of the pillars and instead had to cover them by growth from the sides. The magnetic hysteresis loops of BFO-covered BFO–CFO (Figure 4c) were independent of BFO blocking layer thickness because the BFO overlayers did not influence the magnetic properties of the spinel pillars.

The morphology of subsequent layers of spinel-perovskite on the BFO-capped BFO–CFO was highly dependent on whether the CFO pillars were fully covered by the BFO layer. Figure 4d,e show top view SEM images of BFO–MFO nanocomposites on BFO-blocked BFO–CFO (BFO–(CFO/BFO/MFO)). In both cases the spinel pillars showed the same crystallographic orientation but the BFO matrix showed more voids for the partly-covered case (Figure 4e). Additionally, when the total thickness of the nanocomposite exceeded 120 nm a new phase which corresponded to the dark contrast regions in Figure 4f was formed. This phase did not appear in thick films of nanocomposite without the BFO blocking layer. From the composition analysis, the phase was Fe-rich and was well matched to hematite (JCPDS#00–001–1053) according to XRD (open circle in bottom part of Figure 4f). Hematite is an antiferromagnet which would not contribute to the magnetic hysteresis.

Figure 4g gives a cross-section SEM image of the BFO–(CFO/BFO/MFO) sample in Figure 4a with a 35 nm BFO blocking layer. The positions of the upper layer of MFO pillars were uncorrelated with the positions of the bottom CFO pillars as a result of the BFO layer. The second image in Figure 4g is a cross-sectional low magnification TEM Z-contrast image of the same sample. The BFO matrix is bright due to the high-Z Bi. EDS element analysis for the BFO matrix, bottom pillar and top pillar are shown. The matrix consisted of Bi, Fe, and O. Mg around 1.26 keV of energy was only detected in the top pillar. The Co peak is close to the Fe peak but was stronger in the bottom pillar. Bi was seen at both pillar sites because the TEM sample was thicker than the pillar diameter, so BFO matrix remained in front or behind the spinel pillars. According to the composition mapping, Figure S6 (Supporting Information), there was no detectable diffusion of Bi into spinel nor of Co and Mg into the perovskite phase. Figure 4h,i are HRTEM images around the STO/CFO and BFO/MFO interfaces, respectively. The sample was cut along the [110] in-plane direction and the normal direction is $[\bar{1}10]$, which makes it possible to observe (*lll*) and (*l*00) planes meeting at an angle of 55°. The (*lll*) and (2*l*,2*l*,2*l*) planes of perovskite and spinel phases were parallel to each other as expected from the epitaxial growth.

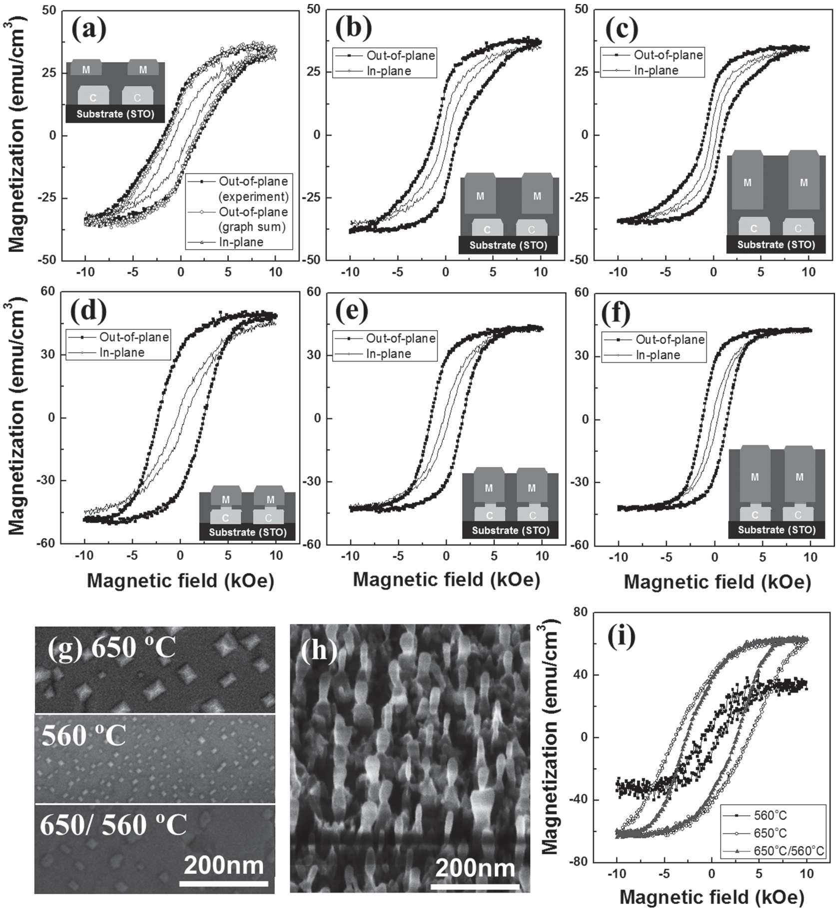

Figure 5. Room temperature measured in-plane and out-of-plane hysteresis loops of various thickness MFO pillars in a BFO matrix grown on different thicknesses of BFO-blocked BFO–CFO nanocomposite. The height of the MFO pillars was a,d) 80 nm; b,e) 120 nm; and c,f) 160 nm. The blocking layer of BFO was 35 nm in (a–c) (i.e., minimum separation between top of CFO and bottom of MFO was 20 nm) while in (d–f) the BFO blocking layer was 20 nm and the CFO and MFO are in contact. The insets show the structures schematically. g) Top view SEM images of BFO–CFO nanocomposite fabricated at 560 °C, 650 °C and two different temperature steps of 650/560 °C. h) 45° tilted SEM image of the BFO–CFO nanocomposite deposited at 650/560 °C after etching in HCl for 180 s. i) Out-of-plane hysteresis loop comparison of the three BFO–CFO nanocomposites in (g).

In comparison, a Z-contrast image of a BFO-(CFO/MFO) sample with a thin BFO blocking layer showed connections between the CFO and MFO pillars (Figure 4j). The MFO pillars formed directly above the CFO pillars. Composition analysis showed the dispersion of Mg and Co throughout the top and bottom pillars suggesting that the small contact area provided a path for diffusion.

Figure 5a–f shows the magnetic hysteresis loops for BFO–(CFO/BFO/MFO) bi-pillar nanocomposites. In Figure 5a, the BFO blocking layer was 35 nm, leading to 20 nm separation between the top of the CFO and the bottom of the MFO pillars, whereas in Figure 5d the CFO and BFO were in contact (BFO layer = 15 nm). The magnetic behavior changed significantly compared to the bi-pillar nanocomposite without the blocking layer (Figure 3c). Figure 5a shows changes in slope of the hysteresis loop indicating the reversal of a soft (around zero field) and a hard magnetic component. The low field step had a small amplitude due to the low moment of MFO, but the loop for the composite matched very well to a loop calculated by summing the loops of individual BFO–MFO and BFO–CFO samples from Figure 2. On the other hand, the magnetic hysteresis loops of the bi-pillar composite whose spinel pillars were connected, Figure 5d, showed no evidence of steps or of distinct switching of a hard and soft component. The loop resembled that of the BFO–(CFO/MFO) without any BFO blocking layer, Figure 3c, even though the contact area between the CFO and MFO pillars was small.

Manipulation of the magnetic hysteresis loops was also demonstrated by changing the thickness of the soft layer in the bi-pillar. Because the saturation magnetic moment of MFO is small, we fabricated thicker MFO pillars on a constant CFO thickness to increase the MFO fraction. The height of the MFO pillars was 120 nm in Figure 5b,e and 160 nm in Figure 5c,f, while the thickness of CFO was fixed at 50 nm. As the MFO pillar thickness increased the low-field step became more prominent and the coercivity of the composite was reduced. In contrast, for pillars where the CFO and MFO were in contact, raising the MFO thickness led to an overall decrease in coercivity.

Finally, to tune the magnetic hysteresis loop by changing the pillar shape, we fabricated BFO–CFO nanocomposites by growing layers at two different temperatures. We found that small width pillars having isotropic magnetic loops were formed at 560 °C due to the different strain imposed by low-temperature BFO. We therefore expect that pillar shape and magnetic properties can be controlled when low temperature deposited pillars are stacked on BFO–CFO grown at high temperatures, avoiding issues of interdiffusion since the pillar composition is fixed. The three top view SEM images in Figure 5g show BFO–CFO nanocomposites fabricated at 650 °C, 560 °C and two different temperatures of 650/560 °C, respectively. When the BFO–CFO nanocomposite was formed at two different temperatures, the top of the pillar had an intermediate diameter and the pillars after etching showed a bowling pin shape (Figure 5h). By changing the shape of the pillars the magnetic properties can be tuned, yielding lower coercivity and a lower saturation field. This opens possibilities for well controlled self-assembled heteroepitaxial multiferroic devices.

3. Conclusions

To summarize, most work on two-phase oxide nanocomposites has focussed on structures which are uniform in the out-of-plane direction. The present results show that it is possible to modulate the structures in the out-of-plane direction by changing the composition of the targets, the layer sequence or the substrate temperature during growth, producing a film which is heterogeneous in three dimensions. It is challenging to produce compositionally-modulated spinel pillars due to the high interdiffusion of cations such as Mg, Co, and Ni in the spinel structure at the growth temperature of ≈650 °C, and growth at much lower temperatures to suppress interdiffusion produced unwanted phases. To create diffusion barriers within the pillars, blocking layers of BFO were incorporated forming BFO–(CFO/BFO/MFO) nanocomposites. For a sufficient BFO thickness, here ≈35 nm, the bottom layer of CFO pillars was fully coated and a further layer of MFO pillars could be grown without interdiffusion between the CFO and MFO. The upper MFO pillars did not form directly above the lower CFO pillars. In contrast, when the BFO blocking layer was thinner, the tops of the CFO pillars protruded and formed nucleation sites for the upper MFO pillars, but also provided a path for cation interdiffusion within the CFO/MFO bipillars.

The magnetic hysteresis of the nanocomposite was sensitive to the morphology and strain state of the spinel phase. BFO–CFO nanocomposites were magnetically hard with a high out-of-plane anisotropy as a result of both shape and magnetoelastic anisotropy arising from the high magnetoelastic coefficients of CFO, while BFO–MFO (where MFO has low magnetoelastic coefficients) and BFO–NFO (where NFO has low strain) were much softer. For BFO–(CFO/BFO/MFO) with decoupled MFO and CFO pillars, the hysteresis loop corresponded to a superposition of the hysteresis loops of BFO–CFO and BFO–MFO nanocomposites with two different switching fields. However, for BFO–(CFO/BFO/MFO) with coupled, interdiffused MFO/CFO pillars, the hysteresis loop indicated only one switching field and the coercivity was intermediate between the coercivity of BFO–CFO and BFO–MFO. An alternative way to manipulate the coercivity and anisotropy of the nanocomposites was to vary the deposition temperature leading to a width-modulated structure. These results show that control over self-assembled nanocomposites in the out-of-plane direction can be obtained. Combining this with templating of the pillar locations[47] could allow complex 3D heterostructures to be produced with well defined magnetic, ferroelectric or other properties.

4. Experimental Section

Fabrication Process: $CoFe_2O_4$, $MgFe_2O_4$, and $NiFe_2O_4$ targets were prepared by a conventional oxide sintering method. The powders calcined at 1100 °C and spinel targets sintered at 1300 °C were single phase spinel without any secondary phases according to one dimensional powder X-ray diffraction. The lattice parameters of the final targets were $a_{CFO} = 8.390 \pm 0.002$ Å, $a_{MFO} = 8.372 \pm 0.002$ Å, and $a_{NFO} = 8.334 \pm 0.003$ Å which agree with the bulk lattice parameters of $a_{bulk,CFO} = 8.392$ Å (JCPDS # 00–022–1086), $a_{bulk,MFO} = 8.375$ Å (JCPDS #00–017–0464), and $a_{bulk,NFO} = 8.338$ Å (JCPDS #01–074–2081).

CPLD was used to produce samples with a range of compositions and to optimize the deposition conditions. Detailed combinatorial deposition methods are described elsewhere.[9,27,28] Targets were ablated with a KrF laser (wavelength of 248 nm) with a fluence of 2.6 J cm^{-2} and a repetition rate of 10 Hz on (001) $SrTiO_3$ (STO, $a_{bulk,STO} = 3.905$ Å) substrates. Films were deposited at 650 °C substrate temperature and 5 mTorr oxygen pressure. Vertical nanocomposite films were made by alternately depositing a sub-monolayer thickness of each material. To change the spinel composition part way through deposition the spinel target was exchanged with a target of different composition without interrupting the process. In order to avoid cation diffusion, some films were deposited at low temperatures of 480–600°C and additional barrier layers of MgO ($a_{bulk,MgO} = 4.213$ Å), which has half the lattice parameter of spinel ferrites, and $MgAl_2O_4$ (MAO, $a_{bulk,MAO} = 8.083$ Å) which is a nonmagnetic spinel, were introduced.

Characterization of Structure and Magnetic Properties: Structure was investigated by X-ray diffraction (XRD, Rigaku D/MAX-R) and high resolution X-ray diffraction (HRXRD, Bruker-AxsD8). In-plane and out-of-plane lattice parameters were obtained from asymmetric reciprocal space mapping (RSM) using HRXRD. Top view images of the nanocomposites were observed by scanning electron microscopy (SEM, Helios Nanolab 600). To observe freestanding pillars, some samples were etched with 10% dilute hydrochloric acid (HCl) and rinsed with DI water to remove the BFO.

The vertical growth morphology and composition analysis were carried out using high resolution transmission electron microscopy (HR-TEM, JEOL JEM 2010) and energy dispersive spectroscopy (EDS) in the TEM. For the investigation of pillar growth and cation diffusion, the nanocomposite film was etched in HCl to remove the BFO and the released pillars were gathered on a copper mesh coated with a carbon film using a syringe after diffusing in isopropyl alcohol. For cross-sectional observation, TEM samples were prepared by focused ion beam (FIB) milling. An Au layer was sputtered over the film to make a conduction path and Pt was deposited in the FIB chamber on the target area to avoid damage from the ion beam, before cutting a section with the FIB and transferring it to a grid. The magnetic properties of films were measured using vibrating sample magnetometry (VSM, ADE model 1660) at room temperature and magnetization was normalized by the net volume of the films instead of the volume of the magnetic spinel, due to uncertainty in the spinel volume fraction.

Supporting Information

Supporting Information is available from the Wiley Online Library or from the author.

Acknowledgements

This work was supported by NSF Division of Materials Research and the FAME Center, one of six STARnet Centers supported by the Semiconductor Research Corporation and DARPA. Facilities from CMSE, an NSF MRSEC, DMR0819762, were used.

Received: August 13, 2013
Revised: October 22, 2013
Published online: December 11, 2013

---

[1] H. Zheng, J. Wang, S. E. Lofland, Z. Ma, L. Mohaddes-Ardabili, T. Zhao, L. Salamanca-Riba, S. R. Shinda, S. B. Ogale, F. Bai, D. Viehland, Y. Jia, D. G. Schlom, M. Wuttig, A. Roytburd, R. Ramesh, *Science* **2004**, *303*, 661.
[2] S. M. Wu, S. A. Cybart, P. Yu, M. D. Rossell, J. X. Zhang, R. Ramesh, R. C. Dynes, *Nat. Mater.* **2010**, *9*, 756.
[3] A. Ohtomo, H. Y. Hwang, *Nature* **2004**, *427*, 423.
[4] J. Chakhalian, J. W. Freeland, G. Srajer, J. Strempfer, G. Khaliullin, J. C. Cezar, T. Charlton, R. Dalgliesh, C. Bernhard, G. Cristiani, H.-U. Habermeier, B. Keimer, *Nat. Phys.* **2006**, *2*, 244.
[5] J. Li, I. Levin, J. Slutsker, V. Provenzano, P. K. Schenck, R. Ramesh, J. Ouyang, A. L. Royburd, *Appl. Phys. Lett.* **2005**, *87*, 072909.

[6] S.-C. Liao, P.-Y. Tsai, C.-W. Liang, H.-J. Liu, J.-C. Yang, S.-J. Lin, C.-H. Lai, Y.-H. Chu, *ACS Nano* **2011**, *5*, 4118.
[7] Q. Zhan, R. Yu, S. P. Crane, H. Zhang, C. Kisielowski, R. Ramesh, *Appl. Phys. Lett.* **2006**, *89*, 172902.
[8] D. H. Kim, N. M. Aimon, C. A. Ross, *J. Appl. Phys.* **2013**, *113*, 17B510.
[9] R. M. Bozorth, E. F. Tilden, A. J. Williams, *Phys. Rev.* **1955**, *99*, 1788.
[10] J. Wang, J. B. Neaton, H. Zheng, V. Nagarajan, S. B. Ogale, B. Liu, D. Viehland, V. Vaithyanthan, D. G. Scholm, U. V. Waghmare, N. A. Spaldin, K. M. Rabe, M. Wuttig, R. Ramesh, *Science* **2003**, *299*, 1719.
[11] F. Zavaliche, T. Zhao, H. Zheng, F. Straub, M. P. Cruz, P.-L. Yang, D. Hao, R. Ramesh, *Nano Lett.* **2007**, *7*, 1586.
[12] N. M. Aimon, J. Liao, C. A. Ross, *Appl. Phys. Lett.* **2012**, *101*, 232901.
[13] R. Comes, H. Liu, M. Khokhlov, R. Kasica, J. Lu, S. A. Wolf, *Nano Lett.* **2012**, *12*, 2367.
[14] E. F. Kneller, R. Hawig, *IEEE Trans. Magn.* **1991**, *27*, 3588.
[15] Y. Wang, Y. Huang, Q. Wang, *J. Magn. Magn. Mater.* **2012**, *324*, 3024.
[16] M. A. Radmanesh, S. A. S. Ebrahimi, *J. Magn. Magn. Mater.* **2012**, *324*, 3094.
[17] D. Roy, P. S. A. Kumar, *J. Appl. Phys.* **2009**, *106*, 073902.
[18] E. E. Fullerton, J. S. Jiang, M. Grimsditch, C. H. Sowers, S. D. Bader, *Phys. Rev B.* **1998**, *58*, 12193.
[19] H. Zeng, J. Li, J. P. Liu, Z. L. Wang, S. Sun, *Nature* **2002**, *420*, 395.
[20] A. J. Zambano, H. Oguchi, I. Takeuchi, Y. Choi, J. S. Jiang, J. P. Liu, S. E. Lofland, D. Josell, L. A. Bendersky, *Phys. Rev B.* **2007**, *75*, 144429.
[21] D. Navas, J. Torrejon, F. Béron, C. Redondo, F. Batallan, B. P. Toperverg, A. Devishvili, B. Sierra, F. Castaño, C. R. Pirota, C. A. Ross, *New J. Phys.* **2012**, *14*, 113001.
[22] Y. Suzuku, R. B. Van Dover, E. M. Gyorgy, J. M. Phillips, R. J. Felder, *Phys. Rev B.* **1996**, *53*, 14016.
[23] A. V. Ramos, S. Matzen, J.-B. Moussy, F. Ott, M. Viret, *Phys. Rev B.* **2009**, *79*, 014401.
[24] C. A. Kleint, M. K. Krause, R. Höhne, T. Walter, H. C. Semmelhack, M. Lorenz, P. Esquinazi, *J. Appl. Phys.* **1998**, *84*, 5097.
[25] M. G. Chapline, S. X. Wang, *J. Appl. Phys.* **2005**, *97*, 10C915.
[26] X. Lu, Y. Kim, S. Goetze, X. Li, S. Dong, P. Werner, M. Alexe, D. Hesse, *Nano Lett.* **2011**, *11*, 3202.
[27] D. H. Kim, L. Bi, N. M. Aimon, P. Jiang, G. F. Dionne, C. A. Ross, *ACS Comb. Sci.* **2012**, *14*, 179.
[28] N. M. Aimon, D. H. Kim, H. K. Choi, C. A. Ross, *Appl. Phys. Lett.* **2012**, *100*, 092901.
[29] R. K. Mishra, G. Thomas, *J. Appl. Phys.* **1977**, *48*, 4576.
[30] H. Zheng, Q. Zhan, F. Zavaliche, M. Sherburne, F. Straub, M. P. Cruz, L.-Q. Chen, U. Dahmen, R. Ramesh, *Nano Lett.* **2006**, *6*, 1401.
[31] J. L. MacManus-Driscoll, P. Zerrer, H. Y. Wang, H. Yang, J. Yoon, A. Fouchet, R. Yu, M. G. Blamire, Q. X. Jia, *Nat. Mater.* **2008**, *7*, 314.
[32] N. Dix, R. Muralidharan, J. Guyonnet, B. Warot-Fonrose, M. Varela, P. Paruch, F. Sánchez, J. Fontcuberta, *Appl. Phys. Lett.* **2009**, *95*, 062907.
[33] J. L. MacManus-Driscoll, *Adv. Funct. Mater.* **2010**, *20*, 2035.
[34] H. Zheng, J. Wang, L. Mohaddes-Ardabili, M. Wuttig, L. Salamanca-Riba, D. G. Schlom, R. Ramesh, *Appl. Phys. Lett.* **2004**, *85*, 2035.
[35] M. Foster, M. Iliev, D. Nix, X. Martí, M. Barchuk, F. Sánchez, J. Fontcuberta, *Adv. Mater.* **2012**, *22*, 4344.
[36] Y. Suzuki, R. B. Van Dover, E. M. Gyorgy, J. M. Phillips, V. Korenivski, D. J. Werder, C. H. Chen, R. J. Felder, R. J. Cava, J. J. Krajewski, W. F. Peck, *J. Appl. Phys.* **1996**, *79*, 5923.
[37] I. Stern, J. He, X. Zhou, P. Silwal, L. Miao, J. M. Vargas, L. Spinu, D. H. Kim, *Appl. Phys. Lett.* **2011**, *99*, 082908.
[38] M. W. Barsoum, *Fundamentals of Ceramics*, Taylor & Francis group, New York, USA **2003**.
[39] A. B. Smith, R. V. Jones, *Appl. Phys.* **1966**, *37*, 1001.
[40] J. Van Den Boomgaard, D. R. Terrell, R. A. J. Born, H. F. J. I. Giller, *J. Mater. Sci.* **1974**, *9*, 1705.
[41] N. Keller, A. Das, M. Guyot, M. Porte, R. Krishnan, *Solid State Commun.* **1998**, *105*, 333.
[42] P. D. Thang, G. Rijnders, D. H. A. Blank, *J. Magn. Magn. Mater.* **2007**, *310*, 2621.
[43] C. Fei, Y. Zhang, Z. Yang, Y. Liu, R. Xiong, J. Shi, X. Ruan, *J. Magn. Magn. Mater.* **2011**, *323*, 1811.
[44] S. Schnittger, C. Jooss, S. Sievers, *J. Phys.: Conf. Ser.* **2010**, *200*, 072086.
[45] T. Sakamoto, K. Okada, A. N. Hattori, T. Kanki, H. Tanaka, *Nanotechnology* **2012**, *23*, 335302.
[46] T. Sakamoto, K. Okada, A. N. Hattori, T. Kanki, A. S. Borowiak, B. Gautier, B. Vilquin, H. Tanaka, *J. Appl. Phys.* **2013**, *113*, 104302.
[47] N. M. Aimon, H. K. Choi, X. Sun, D. H. Kim, C. A. Ross, unpublished.